

# Hydrodynamic Insight Drives Multimodal Vortex-Field Dynamics via Streamline Engineering

*Wenxiang Yan,<sup>1,2,†</sup> Zheng Yuan,<sup>1,2,†</sup> Yuan Gao,<sup>1,2</sup> Zhaozhong Chen,<sup>4</sup> Zhi-Cheng Ren,<sup>1,2</sup> Xi-Lin Wang,<sup>1,2</sup> Jianping Ding,<sup>1,2,3,\*</sup> and Hui-Tian Wang<sup>1,2,\*</sup>*

<sup>1</sup>National Laboratory of Solid State Microstructures and School of Physics, Nanjing University, Nanjing 210093, China

<sup>2</sup>Collaborative Innovation Center of Advanced Microstructures, Nanjing University, Nanjing 210093, China

<sup>3</sup>Collaborative Innovation Center of Solid-State Lighting and Energy-Saving Electronics, Nanjing University, Nanjing 210093, China

<sup>4</sup>James Watt School of Engineering, University of Glasgow, Glasgow, G12 8QQ, UK

<sup>†</sup>These authors contributed equally to this work.

\*Corresponding author: jpding@nju.edu.cn; htwang@nju.edu.cn

## Abstract

Since the 1970s, analogies between laser dynamics and (super)fluid systems have elucidated phenomena from superconductivity to Bose–Einstein condensation. Inspired by Coulet et al.’s 1989 formalization of optical vortices via hydrodynamic whirlpools, we here advance a hydrodynamic paradigm for vortex-beam propagation. By treating the Poynting-vector trajectories as “energy streamlines,” we establish a three-dimensional map of photon trajectories and energy flow. Angular-spectrum engineering in momentum space, together with the fluid-continuity equation, is used to sculpt these streamlines and thereby tailor multimodal, independently tunable propagation behaviors. The resulting beams simultaneously suppress diffraction- and OAM-induced broadening and inherit the diffraction-free, self-healing, self-accelerating, and self-similar traits of classic structured modes, with adjustable energy-density profiles to compensate loss. Optical-tweezer measurements—akin to particle-tracking velocimetry of fluid dynamics—confirm that trapped microspheres trace the prescribed streamlines, laying the groundwork for future precision three-dimensional photonic manipulation. In a free-space communication case study, streamline-engineered multimodal vortex beams deliver an order-of-magnitude increase in independent channels, enhanced turbulence resilience, and non-line-of-sight capability. This hydrodynamic framework thus furnishes a versatile, experimentally verified toolkit for multimodal control of vortex beams and substantially broadens their application scope, while opening new avenues for fluid dynamics simulations using optical analogues.

## Introduction

Structured light beams<sup>1,2</sup>, as solutions of the Helmholtz equation, propagate in free space with intriguing dynamics. Since the advent of the laser, Gaussian-mode beams — including fundamental, Hermite–Gaussian, Laguerre–Gaussian, and Ince–Gaussian modes<sup>3,4</sup>— exhibit self-similar diffraction: their transverse profile remains invariant apart from overall scaling. In contrast, Bessel beams<sup>5</sup> are diffraction-free and self-healing, inspiring variants such as cosine<sup>6</sup>, Mathieu<sup>7</sup>, and parabolic beams<sup>8</sup> that reconstruct after perturbation. Airy beams, which bear a caustic phase<sup>9</sup>, combine non-diffraction and self-healing with transverse parabolic acceleration<sup>10,11</sup>, and have led to a spectrum of paraxial and non-paraxial accelerating beams<sup>12</sup>, as well as abruptly autofocusing modes<sup>13</sup>. Despite these innovations, classical structured beams—Laguerre–Gaussian,

Bessel, and Airy—retain fixed propagation laws (e.g., Airy beams accelerate only along a predetermined parabola, and Gaussian modes diverge hyperbolically), limiting their versatility. *To meet the demands of complex applications, it is essential to develop new theoretical frameworks and adaptive manipulation techniques that can simultaneously tailor multimodal propagation characteristics, thereby expanding the functional boundaries of structured light*<sup>1,2</sup>.

Higher-order Laguerre–Gaussian beams possess an azimuthal phase gradient that imparts a helical wavefront and a central ring-shaped intensity null, forming “optical vortices” that carry orbital angular momentum (OAM) proportional to the topological charge<sup>14,15</sup>. Over the past three decades, these beams have garnered significant interest for applications in optical manipulation, information transfer, and quantum computation<sup>16,17</sup>. Despite their promise, two intrinsic propagation issues impede their broader utility. *First, higher OAM orders cause pronounced beam expansion and increased divergence, undermining their use in spatial-division multiplexing, fiber-based transmission, and particle trapping*<sup>18–20</sup>. *Second, conventional vortex fields succumb to diffraction-induced broadening over long distances*<sup>21–23</sup>, *limiting performance in long-range communication, sensing, imaging, and quantum information tasks*. For example, in zero-radial-index Laguerre–Gaussian modes<sup>24</sup>, the beam radius scales as  $r(|l|, z) = w_0 \sqrt{(|l|+1)} \sqrt{1 + (z/z_0)^2}$ , where  $l$ ,  $w_0$  and  $z_0$  denote the topological charge, beam waist and Rayleigh distance, respectively. Although specialized designs—such as perfect vortex beams<sup>25</sup>, Bessel vortex beams<sup>5</sup>, and iso-propagation vortex modes<sup>26,27</sup> with OAM-independent propagation—can mitigate one of these transmission constraints, none concurrently overcomes both.

In this work, a hydrodynamic framework is introduced for the multimodal manipulation of vortex-beam propagation dynamics. Exploiting the theoretical analogy between fluid flows and electromagnetic fields, energy streamlines—the three-dimensional trajectories defined by the Poynting vector—are adopted as intuitive guides for photon motion and energy transport in free space. Momentum-space angular-spectrum engineering, combined with the “fluid continuity equation”, enables precise sculpting of these streamlines to prescribe multimodal, independently tunable propagation behaviours. This hydrodynamic strategy simultaneously suppresses both diffraction- and OAM-induced broadening, yielding a non-diffracting perfect vortex beam whose “donut” size remains invariant with respect to topological charge and propagation distance. Furthermore, these novel vortex beams can be endowed with multimodal dynamics—a tailored combination of hallmark features: the diffraction-free and self-healing behaviour of Bessel beams, the OAM-invariant evolution of iso-propagation modes, the adjustable self-similarity of Laguerre–Gaussian beams, and the custom self-acceleration of Airy beams, all while permitting tunable energy delivery to offset attenuation. Optical-tweezer measurements, analogous to particle-tracking velocimetry in fluid dynamics, confirm that trapped microspheres faithfully follow the designed energy streamlines, thereby validating the hydrodynamic model and furnishing a route to precision three-dimensional photonic manipulation. In free-space communication trials, streamline-engineered multimodal vortex beams provide an order-of-magnitude increase in independent channels, reduced turbulence-induced mode scattering, and dynamic non-line-of-sight operation. Collectively, this hydrodynamic framework offers a comprehensive, experimentally verified toolkit for tailoring multimodal vortex-beam dynamics and extends the functional envelope of structured light.

## Results

### Hydrodynamic Analogy: Mapping Light Propagation through Streamline Dynamics

The striking parallel between laser dynamics and fluid or superfluid behavior dates back to the early

1970s, when laser-physics equations were recast into the form of the complex Ginzburg–Landau equations<sup>28</sup>. Since then, this unifying framework has provided deep insight into a host of phenomena—from superconductivity and superfluidity to Bose–Einstein condensation<sup>29</sup>. Motivated by these connections, researchers have probed the hydrodynamic character of optical fields, revealing a wealth of nonlinear behaviors—chaos, multistability, and even turbulence—predicted theoretically and confirmed experimentally in laser systems<sup>30–35</sup>. A pivotal moment arrived in 1989, when Couillet et al., inspired by fluid vortices, formally introduced the notion of optical vortices<sup>15</sup>, catalyzing the modern exploration of structured light. Building on this heritage, we now broaden the fluid–optics analogy to describe light propagation through the lens of flow fields and streamlines.

In classical fluid dynamics, the Eulerian description characterizes the fluid’s motion via a velocity field  $\mathbf{v}(\mathbf{R}, t)$ , where  $\mathbf{R} = \{x, y, z\}$  denotes spatial position. By integrating this field with the hydrodynamic differential equations, one visualizes the flow using streamlines—trajectories whose tangent at each point aligns with the local velocity. Formally, if  $\mathbf{R}(z, t) = \{x(z, t), y(z, t), z\}$ , then its evolution obeys

$$\frac{dx(z, t)}{v_x(\mathbf{R}(z), t)} = \frac{dy(z, t)}{v_y(\mathbf{R}(z), t)} = \frac{dz}{v_z(\mathbf{R}(z), t)} \quad (1)$$

where  $\mathbf{v} = \{v_x, v_y, v_z\}$ . Regions where streamlines cluster correspond to faster flow, whereas sparse regions signify slower motion. This formalism lays the groundwork for mapping optical-field evolution onto an analogous hydrodynamic picture.

In this analogy, a monochromatic light field can be treated as an steady-state unchanging flow field ( $\partial \mathbf{v} / \partial t = 0$ ), where its “velocity field” is represented by the momentum distribution of light—quantified by the Poynting vector<sup>36</sup>. Specifically, for a scalar wave  $\psi(\mathbf{R})$ , the Poynting vector  $\mathbf{p}(\mathbf{R})$ —the local expectation value of the momentum operator—is given by

$$\mathbf{p}(\mathbf{R}) = \text{Im} \psi^*(\mathbf{R}) \nabla \psi(\mathbf{R}) = |\psi(\mathbf{R})|^2 \nabla \arg \psi(\mathbf{R}), \quad (2)$$

By substituting this momentum distribution (Poynting vectors) into Eq. (1), the energy streamlines of the optical field — “roadmap” of photon motion — can be derived, which is the streamlines of the Poynting vector. These trajectories,  $\mathbf{R}(z) = \{x(z), y(z), z\} = \{r(z), \phi(z), z\}$ , can be determined in Cartesian or cylindrical coordinates by solving the hydrodynamic differential equations<sup>37</sup>:

$$dx(z)/dz = p_x(\mathbf{R}(z))/p_z(\mathbf{R}(z)), \quad dy(z)/dz = p_y(\mathbf{R}(z))/p_z(\mathbf{R}(z)); \quad (3-1)$$

$$dr(z)/dz = p_r(\mathbf{R}(z))/p_z(\mathbf{R}(z)), \quad d\phi(z)/dz = p_\phi(\mathbf{R}(z))/[r(z)p_z(\mathbf{R}(z))]; \quad (3-2)$$

where  $\mathbf{p} = \{p_x, p_y, p_z\} = \{p_r, p_\phi, p_z\}$ . These energy streamlines offer an intuitive picture of light propagation, often likened to the “Bohmian trajectories” that describe experimentally measurable paths of average photon trajectories<sup>37–40</sup>. In quantum physics, the trajectories of the Poynting vector in light (or quantum-mechanical waves) are described as streamlines in the Madelung hydrodynamic

interpretation<sup>41</sup>, which are later regarded as paths of quantum particles in the Bohm–de Broglie interpretation<sup>42,43</sup>.

For Bessel beams<sup>37</sup>, the energy streamlines follow the helical trajectories

$$\mathbf{R}(z) = \{r(z), \varphi(z), z\} = \left\{ r_0, \varphi_0 + \frac{l}{r_0^2 k_{z0}} z, z \right\}, \quad (4)$$

where  $r_0$  and  $\varphi_0$  denote each streamline's initial radial and azimuthal coordinates,  $k_{z0}$  represents the longitudinal wavevector component of the plane waves that constitute the Bessel beam. These paths wrap indefinitely around a cylinder of initial radius  $r_0$  with no radial divergence (Fig. 1C). In contrast, Laguerre–Gaussian beams yield streamlines of the form<sup>37</sup>

$$\mathbf{R}(\zeta) = \{\rho(\zeta), \varphi(\zeta), \zeta\} = \left\{ \rho_0 \sqrt{1 + \zeta^2}, \varphi_0 + \frac{l}{\rho_0^2} \arctan \zeta, \zeta \right\}, \quad (5)$$

in scaled coordinates  $(r, \varphi, z) \equiv (\omega_0 \rho, \varphi, k \omega_0^2 \zeta)$ , where  $k$  donates the wavenumber. Here, each trajectory traces a helix on a hyperboloid, exhibiting pronounced radial spreading (Fig. 1A). These helical energy streamlines vividly illustrate the intrinsic rotational flow characteristic of vortex beams, serving as the hydrodynamic manifestation of optical OAM as introduced by Allen et al.<sup>14</sup>. This unified perspective connects the structured flow of light to a broader class of natural vortex phenomena. Ideally, a complete description of the optical field would require an infinite continuum of energy streamlines, with their local density accurately mapping the spatial variation of light intensity. Ensuring both computational efficiency and visual clarity, we selectively plot a finite number of characteristic streamlines in this work.

By integrating momentum-space angular-spectrum engineering with the optical “fluid-continuity equation”, we sculpt the beam’s momentum field (i. e., velocity fields in hydrodynamic insight) and steer its three-dimensional energy streamlines, thereby deterministically customizing multi-dimensional propagation dynamics (Method 1-3). Compared with traditional geometric-ray methods (e. g., caustics theory) or amplitude–phase/electromagnetic-parameter description, this hydrodynamic framework—conceptualizing light as energy streamlines, furnishes a versatile, experimentally verified toolkit for multimodal control of vortex dynamics and will substantially broadens their application scope.

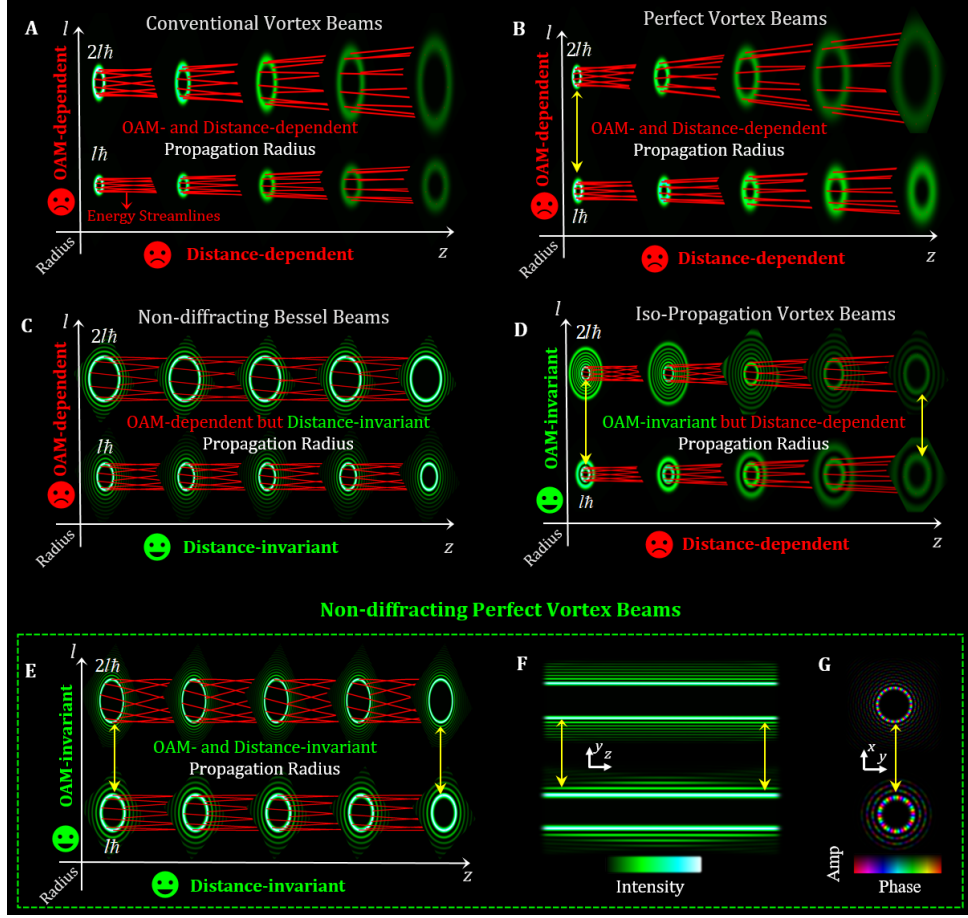


**Fig. 1. Hydrodynamic Depiction for Vortex-beam Propagation Dynamics.** (A) Conventional vortex beams and (B) Perfect vortex beams—radii increase with both OAM and distance; rotation speed of energy streamlines (red curves) slow down over propagation and do not speed up with higher OAM. The yellow double-headed arrow in (B) indicates that perfect vortex fields merely maintain OAM-invariant radii in a single transverse plane. Here,  $lh$  ( $2lh$ ) denotes the OAM per photon. (C) Non-diffracting Bessel beams—radius grows with OAM but stays constant over distance; rotation speed of energy streamlines decelerates as OAM increases but is invariant along propagation. (D) Iso-propagation vortex beams—radius is fixed for all OAM (yellow arrows) but expands with distance; rotation speed of energy streamlines accelerates synchronously with OAM yet decreases as the beam propagates. (E) Non-diffracting perfect vortex beams (NDPVBs)—radius is invariant of both OAM and distance (yellow arrows); rotation speed of energy streamlines accelerates synchronously with OAM and remains constant during propagation. (F) y-z intensity maps and (G) x-y complex-amplitude distributions in plane of the NDPVBs from (E) with  $l = 10$ . The streamlines herein are directly drew from the “streamline” function with the distributions of Poynting vector caculated in Matlab, which are consistent with the analytical solutions from the hydrodynamic differential equations in this work. The demonstration for the streamline rotation speeds can be found in Supplementary Note 4.

### Streamline Engineering: Overcoming Dual Propagation Limits in Vortex Beams

Conventional vortex beams are subject to two interconnected propagation challenges: OAM-induced expansion and diffraction-driven spreading (Fig. 1A: OAM- and distance-dependent propagation radius). These issues limit their effectiveness in optical multiplexing, fiber-optic networks, particle manipulation, and long-distance quantum communication<sup>18,19,23</sup>. Specialized beam designs—

such as perfect vortex beams, high-order Bessel beams, and iso-propagation vortex modes—typically address only one of these challenges. For example, perfect vortex beams<sup>25,27,44</sup> maintain a constant OAM-independent size in a transverse plane but still suffer from both propagation limitations (Fig. 1B: OAM- and distance-dependent propagation radius). Ideal non-diffracting Bessel beams<sup>5</sup> offer a propagation-invariant profile due to their zero divergence angle, yet their size still increases significantly with OAM (Fig. 1C: OAM-dependent but distance-invariant propagation radius). In contrast, iso-propagation vortex beams<sup>26,27</sup> can sustain an OAM-invariant size but experience diffraction-induced divergence as they propagate (Fig. 1D: OAM-invariant but distance-dependent propagation radius). Thus, none of these approaches simultaneously resolves both propagation challenges.

These intertwined propagation limitations can be reinterpreted from a hydrodynamic perspective through the helical streamlines (with the angular speed of  $\omega_z = d\varphi(z)/dz = \varphi'(z)$ ), which not only characterizes the magnitude of the photon's angular momentum but also directly influences the optical forces and momentum exchanged during light-matter interactions<sup>37,45</sup>. The diffraction-induced spreading and OAM-driven expansion of vortex beams cause the attenuation of  $\omega_z$  with both distance and OAM<sup>37,45</sup> (see energy streamlines in Fig. 1 and details demonstrations in Supplementary Note 4). More, specifically, due to the OAM- and distance-dependent beam size, the energy rotation rate  $\omega_z$  does not increase with higher OAM; instead, it tends to decelerate over distance. To simultaneously eliminate both diffraction- and OAM-induced broadening, we sculpt the energy streamlines from non-diffracting Bessel beams (Eq. 4) to the form  $\mathbf{R}(z) = \{r_l, \varphi_0 + l/(r_l^2 k_{zl})z, z\}$ , yielding a non-diffracting perfect vortex beam (NDPVB) whose transverse size  $r_l$  of the innermost ring/mainlobe remains invariant with respect to topological charge  $l$  and propagation distance  $z$  (the subscript “l” indicates “invariant”, Figs. 1E–G). Here,  $k_{zl}$  denotes the customized longitudinal wavevector component of the plane waves constituting the NDPVB, offsetting the expansion with OAM. The energy rotation rate of NDPVBs,  $\omega_z = l/(r_l^2 k_{zl}) \approx l/(r_0^2 k) \propto l$ , accelerates synchronously with increasing OAM while remaining invariant during propagation, thus exhibiting the ideal propagation dynamics of optical vortices, as shown in Fig. 1E. (Methods 1–2 for theoretical framework and experimental generation) Unlike conventional perfect vortex beams that yield a two-dimensional OAM-independent “perfect” ring only within a specific transverse plane and rapidly degrade once off that design plane (Fig. 1B), this non-diffracting perfect vortex beams introduced here constitute the first truly three-dimensional perfect vortices with OAM- and propagation-invariant size and structure (Figs. 1E–G).

### Streamline Sculpting: Tailoring Multimodal Light-Field Dynamics

Structured light beams serve as a powerful platform for advanced photonic applications, offering diverse propagation dynamics that enable new functionalities<sup>1,2</sup>. For example, Airy beams with curved trajectories allow precise beam steering, Gaussian modes with dynamic resizing facilitate adaptable focusing, and non-diffracting, self-healing Bessel beams maintain robust transmission even in challenging conditions.

These behaviors highlight the potential of incorporating such features into vortex beams, whose simple propagation dynamics fall short of the demands of emerging applications. By applying a hydrodynamic approach and strategically configuring energy-streamline trajectories, we can adaptively customize the multimodal propagation dynamics of NDPVBs, expanding their capabilities for complex environments and extending their functional limits.

**Sculpting Streamlines for Adjustable Self-Similar Propagation.** In cylindrical coordinates, the NDPVB's streamlines are reshaped from  $\mathbf{R}(z) = \{r, \varphi_0 + l/(\kappa r^2)z, z\}$  to  $\{r(z), \varphi_0 + l/[\kappa r^2(z)]z, z\}$ , thereby endowing the beam with a dynamically adjustable self-similar radius  $r(z)$  (Figs. 2A–B). The resulting configuration permits precise regulation of the rotational rate, which is given by  $\omega_z(z) = l/[\kappa r^2(z)] \approx l/[\kappa r^2]k$ .

**Sculpting Streamlines for Customized Self-Accelerating Trajectories.** In Cartesian coordinates, the original streamlines  $\mathbf{R}(z) = \{r\cos\varphi(z), r\sin\varphi(z), z\}$  are translated to  $\{x_s(z) + r\cos\varphi(z), y_s(z) + r\sin\varphi(z), z\}$ , where  $\varphi(z) = \varphi_0 + l/(\kappa r^2)z$ , so that propagation follows an arbitrary three-dimensional trajectory  $(x_s(z), y_s(z))$ , thus imparting customizable self-accelerating dynamics to the NDPVB (Figs. 2C–D).

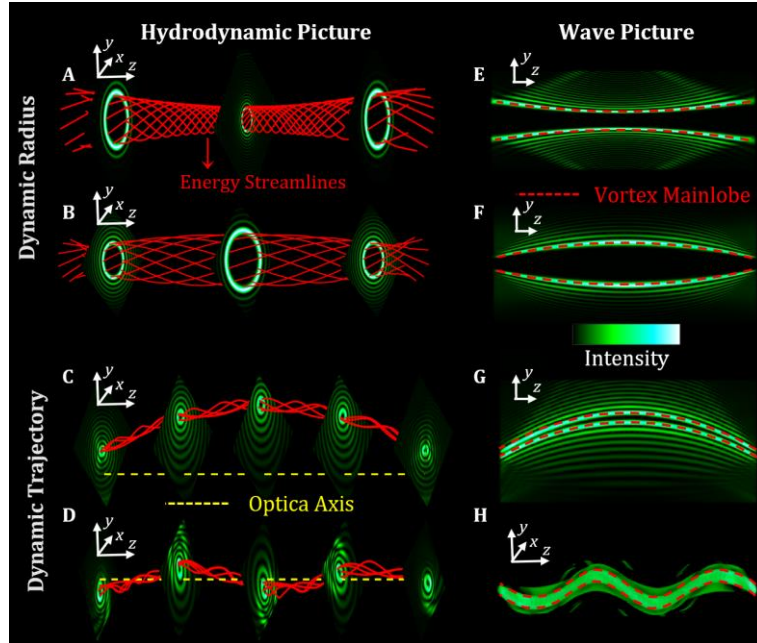


**Fig. 2. Sculpting Streamlines for adjustable self-similarity and customized self-acceleration.** (A, B) NDPVBs with adjustable self-similarity, exhibiting self-shrinking (A) and self-stretching (B) radii; red curves indicate the energy streamlines along the vortex mainlobe. (C, D) NDPVBs with customizable self-accelerating dynamics, propagating along a parabolic (C) and a spiral (D) trajectory. (E–G) Intensity maps of (A–C) in the  $y$ - $z$  plane; red dashed lines denote the vortex mainlobes. (H) Three-dimensional intensity iso-surface corresponding to (D).

**Streamline Interactions Enabling Self-Healing Propagation.** NDPVBs, whose innermost-ring radius remains invariant with respect to topological charge  $l$  and propagation distance  $z$ , are decomposed into two regions: the mainlobe (i.e., region of interest), which carries the highest intensity and governs interactions with matter or detectors, and a series of surrounding sidelobes. The sidelobes sustain and



regulate the propagation dynamics of the mainlobe; together, they constitute the entire beam and account for its total energy. During free-space propagation, main- and sidelobe energy streamlines rotate along their respective cylindrical surfaces without mutual energy exchange. When an obstacle intercepts and truncates the main-lobe streamlines, the sidelobe streamlines spontaneously flow into the mainlobe region upon further propagation, reconstructing both its intensity profile and streamline structure (Fig. 3A). In the absence of these supportive sidelobe streamlines in conventional vortex beams, such spontaneous self-healing cannot occur (see Supplementary Note 5 and Supplementary Movie 1 for details).

**Manipulating Streamline Interactions for Tunable Energy Transfer.** During self-healing, sidelobe streamlines converge into the mainlobe without tunability. By invoking the optical “fluid continuity equation” (Method 3), these sidelobes can be recast as an energy reservoir for the vortex mainlobe. The rate of sidelobe-to-mainlobe streamline transfer can be actively controlled, thereby dynamically adjusting the mainlobe’s spatial energy density to satisfy application-specific intensity requirements. For instance, by directing nearly all sidelobe streamlines into the mainlobe, the local energy density associated with matter or detector interactions can be selectively enhanced (Fig. 3C), yielding improved energy efficiency and signal-to-noise ratios (a case study in Supplementary Note 6 demonstrates a threefold improvement, as well as corresponding experimental results of Supplementary Movie 2). Moreover, by tuning the sidelobe inflow rate, the mainlobe intensity can be held constant across media with different attenuation coefficients, thereby meeting the stringent requirements of imaging and sensing in complex environments under uniform structured-light illumination. In Figs. 3G–J, attenuation profiles were first measured using a fundamental NDPVB in various decay media, and the corresponding optimal sidelobe convergence rates were determined to dynamically compensate for the main-lobe’s energy decay. (Experiment Setup in Supplementary Note 7)



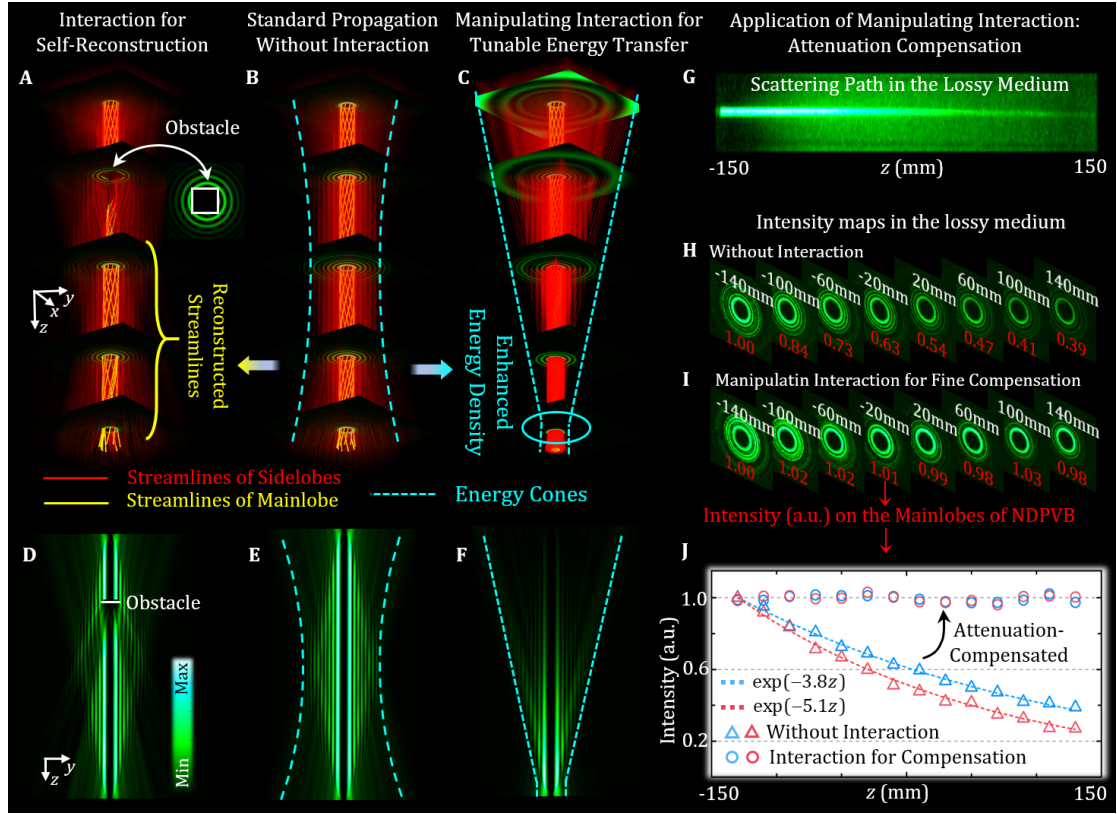


**Fig. 3. Manipulating Streamline Interactions for Self-Healing and Tunable Energy Delivery.** (A) When the mainlobe of a non-diffracting perfect vortex beam (NDPVB) is intercepted by an obstacle (white rectangle), its yellow energy streamlines are truncated. The sidelobe streamlines (red curves) spontaneously flow into the mainlobe region, reconstructing the original streamline structure. (B) In free-space propagation, a standard NDPVB exhibits no interaction between mainlobe and sidelobe streamlines. (C) By actively converging sidelobe streamlines into the mainlobe, the local spatial energy density is enhanced; blue-dotted curves highlight the primary region of energy concentration. (D-F) Intensity maps in the y-z plane corresponding to (A-C), respectively. (G) Attenuated scattered path of a standard NDPVB propagating in a lossy medium (milk suspension). (H) Propagating profiles of the standard NDPVB in the lossy medium, with red font digits indicating the normalized intensity on the mainlobe (blue triangles in (J)), used to probe the attenuation curve (blue-dashed curve in (J)). (I) After adjusting the inflow rate of sidelobe streamlines, the main-lobe intensity remains invariant (blue circles in (J)) despite the medium's attenuation. For a second lossy medium (red-dashed curve in (J)), the probing and dynamically compensated mainlobe intensities are shown by red triangles and red circles, respectively. (J) Attenuation curves for both media (blue- and red-dashed) with corresponding normalized main-lobe intensities: triangles denote unmodified probing NDPVBs and circles denote dynamically compensated NDPVBs.

By precisely sculpting the energy streamlines, multimodal, independently tunable propagation dynamics in optical vortices have been achieved. Within this hydrodynamic framework, both diffraction- and OAM-induced broadening are suppressed, yielding a non-diffracting perfect vortex beam (NDPVB) whose transverse size remains invariant with topological charge and propagation distance. These beams combine the diffraction-free, self-healing properties of Bessel modes, the adjustable self-similarity of Laguerre-

Gaussian modes, and the bespoke self-acceleration of Airy modes, while also allowing tunable energy delivery to counteract attenuation. By directly overcoming the propagation limitations identified in the Introduction, this approach expands the functional boundaries of structured light<sup>1,2</sup>. In the following Sections, we will demonstrate the practical advantages of these streamline-engineered vortices in advanced optical manipulation and in high-performance free-space optical communications.

### **Optical Tweezers as Particle-Tracking Velocimetry: Probing Streamline Dynamics**

In classical particle-tracking velocimetry for fluid dynamics<sup>46</sup>, tracer beads are injected into a flow and their trajectories are recorded by high-speed cameras to reconstruct the underlying streamlines. An analogous strategy was adopted here: microspheres were seeded into the shaped light field, and their motion was captured to map the beam's "streamlines". The optical-tweezers<sup>47</sup> platform (Fig. 4A) was built on an inverted confocal microscope (Nikon TE2000-U) equipped with a 4-f holographic beam-shaping stage housing a reflective spatial light modulator (Holoeye Leto). A continuous-wave laser (Coherent Verdi-V5) was phase-modulated with computer-generated holograms to generate the required multimode vortex fields. These fields interacted with polystyrene microspheres of 2  $\mu\text{m}$  diameter suspended in de-ionized water inside a custom open-top chamber, which comprised an acrylic plate with a through-hole and a glass coverslip forming the base. *The open geometry minimised hydrodynamic resistance and allowed unrestricted particle motion at the water surface. The chamber was mounted on a Nano-LP200 piezo nanopositioner that displaced the liquid-borne microspheres along the optical axis in synchrony with the camera exposure. This coordinated z-scan permitted three-dimensional bead trajectories to be reconstructed with high spatial accuracy.*

Representative measurements (Figs. 4B–D) reveal that tracer-sphere trajectories in 22nd- and 38th-order NDPVBs, as well as in self-similar NDPVB with the linearly expanding radius, adhere closely to the predesigned energy-streamline contours. By contrast, conventional perfect-vortex beams (Fig. 1B) yield a 2D "perfect" ring only within a single transverse plane; once the beam diffracts off that plane, trapped beads escape and trapping ceases (Fig. 4E). In the NDPVB configuration, however, robust three-dimensional trapping and steering within OAM-invariant radii persist over the full axial scan (Figs. 4B and 4C), thereby validating the propagation-invariant, three-dimensional perfect vortex topology. Looking ahead, the combination of smaller probe particles, higher-speed volumetric imaging, and axial-view detection modules<sup>48</sup> promises even finer resolution of energy streamlines. Such advancements will facilitate future true three-dimensional optomechanical control—ranging from microfluidic flow steering and directed cell transport to the assembly of microscale structures<sup>49</sup>—through engineered photon-trajectory sculpting.

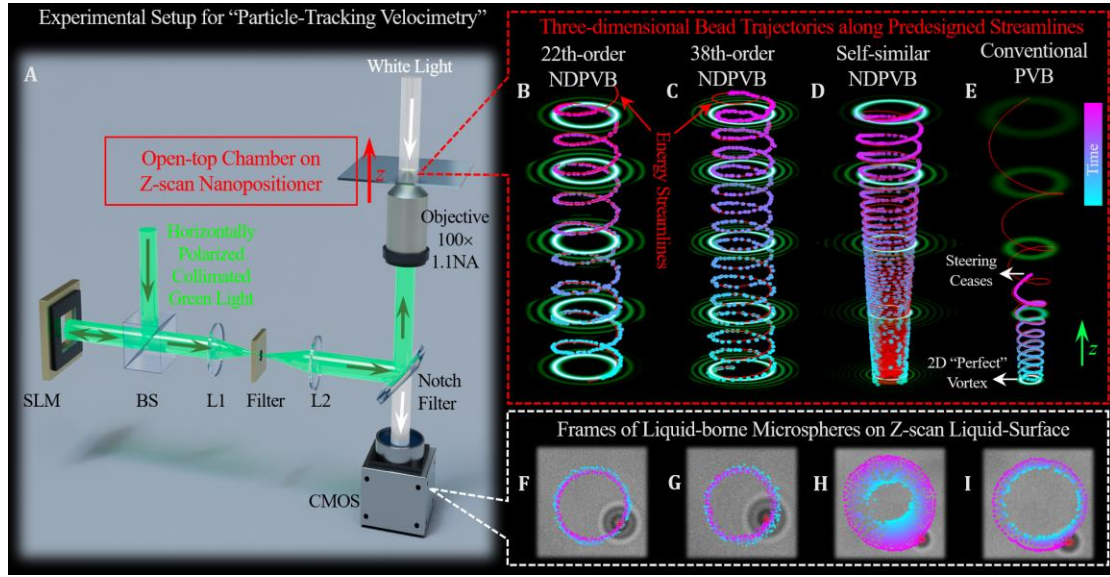


**Fig. 4. Probing Photonic Streamline Dynamics through Optofluidic Velocimetry.** (A) Schematic of the optical tweezers platform for photonic streamline mapping. Key components: beam splitters (BS), phase-only spatial light modulator (SLM), and lens pair (L1-L2). The open-top microfluidic chamber, containing 2  $\mu\text{m}$  polystyrene microspheres in deionized water, was mounted on a Nano-LP200 piezo nanopositioner. Synchronized z-axis displacement and CMOS camera exposure enabled 3D trajectory reconstruction of liquid-borne probing microspheres through coordinated scanning. (B-E) Reconstructed 3D microsphere trajectories (time-color-coded discrete points) in: (B) 22th-order NDPVB, (C) 38th-order NDPVB, (D) self-similar NDPVB with linear radial expansion, and (E) conventional perfect vortex beam. Red curves: Predefined energy streamlines. The conventional beam (E) only maintains 2D “perfect” in a single transverse plane - particles escape and steering ceases when diffracting beyond this plane. (F-I) the CMOS camera frames (Supplementary Movie 3) of liquid-borne probing microspheres on z-scan liquid-surface.

## Streamline-Engineered Vortex Beams: Boosting Capacity and Robustness in Free-Space Communications

In free-space optical-communication architectures, NDPVB—non-diffracting, propagation-invariant vortex beams whose transverse size remains invariant of both OAM order and propagation distance—can support more than an order-of-magnitude increase in mutually orthogonal sub-channels relative to conventional OAM modes (a subset of Laguerre-Gaussian beams with the zero radial index), thereby offering a route toward ultrahigh information capacity (Figs. 5A-5C). When the deleterious influence of atmospheric turbulence on long-haul links, remote sensing and ranging is considered, these beams were verified to experience markedly weaker and more uniform modal scattering than their conventional counterparts—an outcome attributed to the constant, OAM-invariant beam profile maintained along the path (Figs. 5D-5H). By exploiting the customisable self-similar and self-accelerating propagation dynamics inherent to the multimode NDPVB family, the traditional line-of-sight free-space link is generalised to robust non-line-of-sight scenarios (Fig. 6). Together, these features outline a promising framework for next-generation OAM-based free-space optical systems that combine ultrahigh capacity with turbulence resilience and extended

link geometry.

**Streamline-Engineered Vortex Beams for Enhanced Channel Capacity.** Recent advances in information acquisition and processing have underscored the critical role of multiplexing in scaling communication capacity<sup>50</sup>. Optical multiplexing strategies exploiting polarization and wavelength degrees of freedom have significantly extended system bandwidth<sup>51,52</sup>. Among emerging approaches, spatial mode-division multiplexing—where orthogonal spatial modes act as independent channels—has garnered increasing attention<sup>53–55</sup>. In a representative scheme, a free-space optical link combining  $Q$  orthogonal OAM modes, two polarization states, and  $T$  wavelengths yields an aggregate capacity of  $Q \times 2 \times T \times 100$  Gbit/s when each channel carries 100 Gbit/s using quadrature phase-shift keying. This configuration enables petabit-per-second-scale throughput<sup>55</sup>, thereby substantially improving both capacity and spectral efficiency in free-space optical communication systems. Despite its promise, vortex-based spatial mode-division multiplexing encounters notable limitations during free-space propagation. Conventional vortex beams suffer from diffraction-induced spreading and OAM-dependent radial expansion—effects that intensify with increasing topological charge and propagation distance<sup>21,22,24</sup>. As a result, the practical number of accessible spatial subchannels,  $Q$ , is restricted by both the finite aperture of the receiving optics and these propagation limitations<sup>18,19</sup> (Fig. 5A).

To enable a direct comparison among diverse spatial multiplexing schemes, the number of supported individual subchannels,  $Q$ , was evaluated as a function of the system-quality factor<sup>56</sup>  $S = \pi R_0 \times \text{NA} / \lambda$ , where  $R_0$  and NA are the common aperture radius and numerical aperture of both transmitter and receiver, and  $\lambda$  is the wavelength. This dimensionless factor represents the maximum space–bandwidth product a beam can occupy relative to a fundamental Gaussian mode; only modes satisfying this criterion are transmitted, thereby fixing the subchannel count. The resulting approximations for each technique are<sup>56</sup>:  $Q_{\text{OAM}}(S) \approx 2\text{floor}[S] + 1$  for conventional OAM mode multiplexing,  $Q_{\text{LG}}(S) \approx 0.5\text{floor}[S](\text{floor}[S] + 1)$  for Laguerre-gaussian beam multiplexing,  $Q_{\text{HG}}(S) \approx 0.5\text{floor}[S](\text{floor}[S] + 1)$  for Hermite-Gaussian beam multiplexing,  $Q_{\text{MIMO}}(S) \approx \text{round}[0.9S^2]$  for multi-input multi-output transmission,  $Q_{\text{IPVB}}(S) \approx \text{floor}(189.16 \sqrt{S - 0.066})$  for Iso-propagation vortex beam multiplexing<sup>26</sup>, respectively.

By employing the NDPVB basis—which inherently mitigates both diffraction-induced spreading and OAM-driven radial expansion (Fig. 5B)—a substantially expanded set of transmission modes can be accessed beyond those supported by conventional spatial multiplexing, thereby boosting overall link capacity. Exploiting the OAM- and distance-invariant beam profile, the number of NDPVB subchannels is found, via the approach of ref. <sup>56</sup>, to scale as  $Q_{\text{NDPVB}}(S) \approx \text{floor}(569.21 \sqrt{S} - 3)$  (see Supplementary Note 8 for details). Figure 5C shows that, for realistic free-space links with finite apertures and  $S < 30$ , NDPVB multiplexing outperforms all existing schemes in available subchannels. For example, in our proof-of-principle setup ( $S = 6.25$ , Supplementary Note 9),  $Q_{\text{NDPVB}}$  reaches 1419—versus  $Q_{\text{OAM}} = 13$ ,  $Q_{\text{LG}} = Q_{\text{HG}} = 21$ ,  $Q_{\text{MIMO}} = 35$ , and  $Q_{\text{IPVB}} = 471$ —an enhancement ranging from threefold to over a hundredfold. We further evaluated multi-vortex geometric (MVG) beam multiplexing<sup>54</sup>, noting that for  $S < 30$ ,  $Q_{\text{MVG}} \approx Q_{\text{LG}}$  and thus remains below  $Q_{\text{NDPVB}}$ . Although practical capacity also depends on mode-spacing choices and inter-channel crosstalk, a higher

upper bound on  $Q$  directly translates into a larger usable mode set and, typically, increased capacity<sup>18,19</sup>

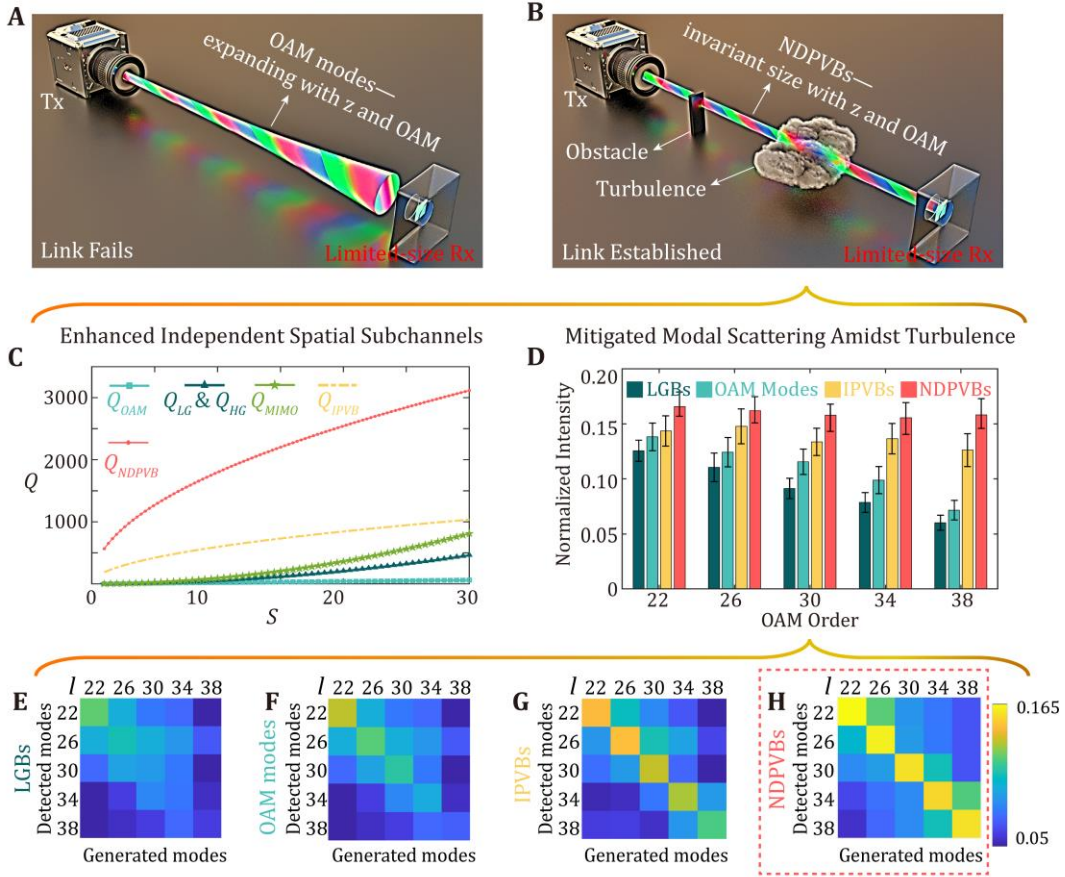


**Fig. 5. Enhanced Capacity and Mitigated Modal Scattering Amidst Atmospheric Turbulence.** (A) In conventional free-space communication, the limited-size receiver (Rx) obstructs OAM modes due to their expansion with propagation distance ( $z$ ) and OAM order, resulting in **Link Fails**. (B) In contrast, NDPVBs maintain an on-demand, invariant size with respect to both  $z$  and OAM, enabling robust transmission and **Link Established** even in the presence of obstacles (self-healing ability) or turbulence. (C) Comparison of the number of independent spatial subchannels supported by various spatial multiplexing techniques, evaluated for system-quality factors ( $S$ ) ranging from 1 to 30. (D–H) Assessment of free-space propagation under atmospheric turbulence for OAM beams, Laguerre-Gaussian beams (LGBs, nonzero-radial-index), iso-propagation vortex beams (IPVBs), and NDPVBs, respectively. The transmission distance is 1000 m with a turbulence strength of  $C_n^2 = 5 \times 10^{-15}$ . Each beam has a consistent waist size while varying its OAM values ( $l = 22, 26, 30, 34, 38$ ). (D) Normalized intensity retained by each initiated mode at  $z = 1000$  m. (E–H) Crosstalk matrices for LGBs, OAM modes, IPVBs, and NDPVBs, providing a quantitative assessment of modal stability across the transmission pathway. Simulation details: propagation distance mesh of 40 m, analysis area of  $0.5 \text{ m} \times 0.5 \text{ m}$ , and turbulence outer and inner scales of 300 m and 0.01 m, respectively. (See Supplementary Note 10 for further details.)

**Streamline Engineering Mitigates Modal Scattering in Turbulent Channels.** Atmospheric turbulence, together with diffraction-induced spreading and OAM-dependent radial expansion, limits both capacity and range in free-space links<sup>1</sup>, and modal scattering grows with increasing turbulence strength or beam diameter increase<sup>57</sup>. As shown in Figs. 5D–5H, streamline-engineering NDPVBs, whose profiles are

invariant to both OAM and propagation distance, exhibit markedly lower and more uniform modal scattering than conventional OAM modes, Laguerre-gaussian beams and iso-propagation vortex beams under the same turbulent conditions. This turbulence resilience cements NDPVBs as ideal carriers for high-capacity, turbulence-robust free-space multiplexing<sup>58</sup>. (See Supplementary Note 10 for details)

**Streamline-Engineered Beams Enable Robust NLOS Communication.** Free-space optical links—whose beam diameters are far smaller than those of radio waves—are prone to interruption by occluders, leading to severe signal loss or complete blackout. Conventional systems thus require an unobstructed line-of-sight (LOS) between transmitter and receiver (Figs. 5A–5B), which restricts their use in complex environments. By contrast, streamline-engineered NDPVBs exploit adjustable self-acceleration and self-similarity to steer around obstacles, extending robust transmission to non-line-of-sight (NLOS) scenarios even under dynamic occlusions (Figs. 6A–6B).

Figures 6C–6N illustrates a high-dimensional NLOS proof-of-principle: a  $128 \times 128$ -pixel true-color “Mandrill” image (24-bit depth) was split into its red, green and blue channels (8 bits each) and mapped onto 24 NDPVB modes with indices  $l = (-60, 60, -55, 55, \dots, -5, 5)$ , using a mode spacing of 5 to suppress crosstalk. Two NLOS channel-engineering cases were tested—self-accelerating trajectory (Case 1) and self-similar radius (Case 2)—to navigate a dynamic occluder (red parts in Figs. 6E, 6G–6J). After demultiplexing (Supplementary Note 9 and Supplementary Movie 4), the image was faithfully reconstructed with bit-error rates of  $2.19 \times 10^{-4}$  (Case 1) and  $8.78 \times 10^{-5}$  (Case 2), both well below the  $3.8 \times 10^{-3}$  forward-error-correction limit (Fig. 6F). In contrast, standard NDPVBs without streamline-engineering multimodal dynamics failed under the same conditions (Figs. 6K–6N). The setup—when using a digital mirror device at 11 kHz—achieved a peak data rate of  $24 \times 11 \text{ k} = 0.264 \text{ Mbit/s}$ . Although our demonstration employed a single occluder due to current modulation limitations of commercial space light modulators, future metasurface platforms should enable even more complex NLOS links. Overall, streamline-engineered NDPVBs with multimodal propagation dynamics marks them as promising carriers for next-generation free-space optical networks that combine ultrahigh capacity, turbulence resilience and robust NLOS transmission.



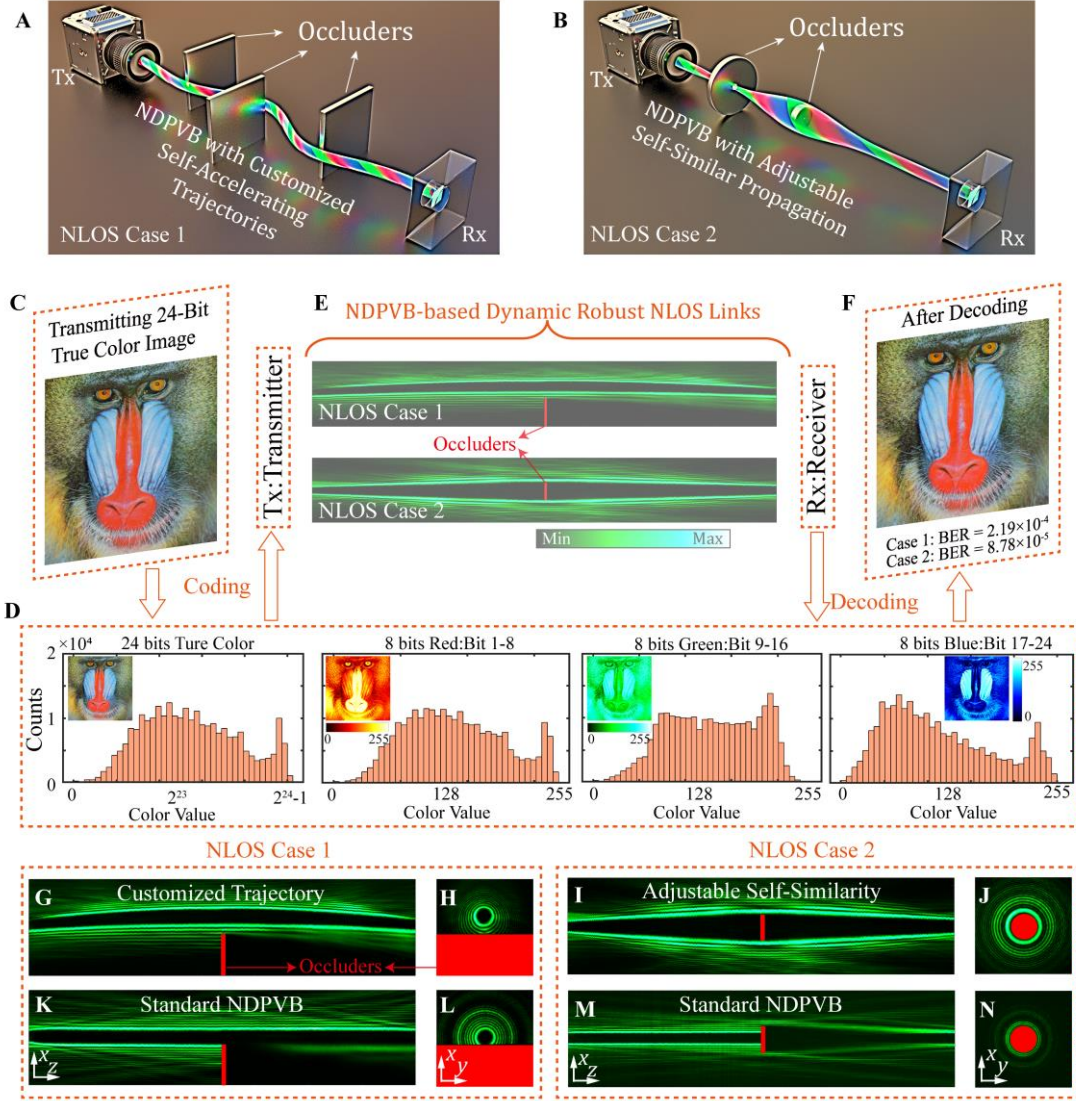


**Fig. 6. NDPVB-multiplexing NLOS image transmission with ultra-high color fidelity.** **A–B.** Schematics of non-line-of-sight channels: when conventional LOS links fail due to multiple occluders fully blocking the receiver, NDPVBs with **(A)** customized self-accelerating trajectories or **(B)** adjustable self-similar expansion navigate around obstacles to restore connectivity. Tx, transmitter; Rx, receiver. **C.** Original true-color “Mandrill” image ( $128 \times 128$  px, 24-bit depth,  $2^{24}$  possible colors). **D.** Color histograms for the full image and its individual red, green and blue 8-bit channels, each mapped to bit-positions 1–24. **E.** Bit-stream mapping: 24 bits per pixel are encoded onto NDPVB modes with indices  $l = (-60, 60, -55, 55, \dots, -5, 5)$  (mode spacing = 5) and carried via (Case 1) self-accelerating or (Case 2) self-similar beams to bypass occlusions (red lines). **F.** Reconstructed “Mandrill” after demultiplexing, showing negligible distortion. Bit-error rates:  $2.19 \times 10^{-4}$  (Case 1) and  $8.78 \times 10^{-5}$  (Case 2), both well under the  $3.8 \times 10^{-3}$  forward-error-correction threshold. **G–J.** Case 1 experimental intensity patterns at the occluder plane: **(G)** streamline-engineered beam self-bends to surmount a wall-shaped mask, **(K)** standard NDPVB is blocked. Corresponding x-y intensity maps are shown in **(H)** and **(L)**, respectively. **K–N.** Case 2 experimental intensity patterns: **(I)** beam with expanded self-similar radius clears a plate-shaped mask, **(M)** standard NDPVB fails. Measured x-y intensity distributions appear in **(J)** and **(N)**. See Supplementary Movie 5 for details of **(G–N)**. The sharp-edged obstacles is produced as masks via the process of photoetching chrome patterns on a glass



substrate (Supplementary Note 11).

## Discussion and Conclusion

Building on the preceding analysis, a hydrodynamic framework for structured light has been established by modeling the optical field as an energy “fluid” and charting its three-dimensional evolution via energy streamlines. Compared with traditional geometric-ray methods (e. g., caustics theory) or amplitude-phase/electromagnetic-parameter description, these streamlines furnish an intuitive, fully three-dimensional roadmap of photon trajectories, simultaneously capturing diffraction, OAM-induced expansion, self-healing, self-acceleration, and self-similarity within a unified framework.

In contrast, conventional structured beams—such as Gaussian modes, Airy beams, or standard vortex beams—are characterized by inherently simple, fixed propagation dynamics; although specialized techniques exist to adjust individual behaviors<sup>59–62</sup>, those methods remain mutually incompatible and insufficient for the multidimensional tailoring demanded by real-world applications. Through the streamline-based approach, both OAM-driven radial expansion and diffraction-induced spreading have been suppressed in concert, giving rise to non-diffracting perfect vortex beams (NDPVBs) with ideal propagation characteristics. Furthermore, by sculpting the underlying streamline geometry, independently tunable multimodal dynamics have been imparted to a single NDPVB: the diffraction-free and self-healing behaviours of Bessel beams, the OAM-invariant evolution of iso-propagation modes, the adjustable self-similarity of Laguerre–Gaussian beams, and the bespoke self-acceleration of Airy beams, all accompanied by controlled energy delivery to offset attenuation.

Validation of the hydrodynamic model has been achieved via optical-tweezer experiments—analogueous to particle-tracking velocimetry in fluid systems—wherein microspheres were observed to faithfully trace the designed streamlines, thus laying the groundwork for future precision three-dimensional photonic manipulation. In free-space communication trials, streamline-engineered multimodal NDPVBs demonstrated an order-of-magnitude increase in independent channels, markedly reduced turbulence-induced mode scattering, and robust non-line-of-sight transmission, thereby positioning them as ideal carriers for next-generation optical networks. Collectively, this hydrodynamic framework bridges fluid dynamics and optical propagation, establishing a versatile, experimentally verified toolkit for multimodal vortex-beam control and charting new directions for structured-light applications in imaging, manipulation, and communication, while opening new avenues for fluid dynamics simulations using optical analogues.

## Method

### 1. Principle of Hydrodynamic framework for Multimodal Propagation Dynamics

The principle of the hydrodynamic framework is outlined in Table 1, where the momentum fields ( $\mathbf{p}(r, \phi, z)$ ) are configured through momentum-space angular-spectrum engineering ( $S(k_r, \phi, k_z)$ ). By solving the hydrodynamic differential equations (Eq. (3)) with the momentum fields, three-dimensional energy streamlines  $\mathbf{R}(z)$  can be sculpted, allowing deterministic control over multimodal propagation dynamics.

The four rows of Table 1 illustrate the manipulation of different propagation behaviors: (1) non-diffracting perfect vortex beams<sup>64</sup> with OAM- and z-invariant radius  $r_l$ , (2) adjustable self-similarity with dynamic radius  $r_l(z)$ , (3) customized self-acceleration with arbitrary trajectory  $(x_s(z), y_s(z))$ , and (4) tunable energy delivery with adjusted energy density  $I(z)$ . Detailed derivations and validations of these concepts can be found in Supplementary Notes 1-2 with Supplementary Movie 6.

Momentum-Space Angular-Spectrum Engineering $S(k_r, \phi, k_z)$	Momentum Fields $\mathbf{p}(r, \phi, z)$ Configuring	Three-dimensional Energy Streamlines $\mathbf{R}(z)$ Sculpting	Multimodal Propagation Dynamics Steering
$A_l e^{il\phi} \mathcal{F}_z \{e^{ik_{zl}z}\}$	$\frac{l}{r_l} \hat{\phi} + k_{zl} \hat{z}$	$\{r_l, \phi_0 + l/(r_l^2 k_{zl})z, z\}$	Non-diffracting Perfect Vortex Beams <sup>64</sup> with OAM- and z- invariant Radius $r_l$
$A_l e^{il\phi} \mathcal{F}_z \{\exp(i \int_{-\infty}^z k_{zl}(z) dz)\}$	$kr'_l(z) \hat{r} + \frac{l}{r_l(z)} \hat{\phi} + k_{zl}(z) \hat{z}$	$\{r_l(z), \phi_0 + l/[r_l^2(z) k_{zl}(z)]z, z\}$	Adjustable Self-similarity with Dynamic Radius $r_l(z)$
$A_l e^{il\phi} \mathcal{F}_z \{e^{ik_x x_s(z) + ik_y y_s(z)} e^{ik_{zl}z}\}$	$kx'_s(z) \hat{x} + ky'_s(z) \hat{y} + \frac{l}{r_l} \hat{\phi} + k_{zl} \hat{z}$	$\{x_s(z) + r_l \cos \varphi(z), y_s(z) + r_l \sin \varphi(z), z\}$	Customized Self-acceleration with Arbitrary Trajectory $(x_s(z), y_s(z))$
$A_l e^{il\phi} \mathcal{F}_z \{\sqrt{I(z)} e^{ik_{zl}z}\}$	$-CI'(z) \hat{r} + I(z) \frac{l}{r_l} \hat{\phi} + I(z) k_{zl} \hat{z}$	Streamline Interaction Manipulation by Optical “Fluid- Continuity Equation”	Tunable Energy Delivery with Adjusted Energy Profiles $I(z)$

**Table 1. Principle of Hydrodynamic framework for Multimodal Propagation Dynamics.** The subscript “z” of “ $\mathcal{F}$ ” refers to the Fourier transform dimensions;  $A_l = \sqrt[3]{3.2823|l| + 4.0849}$  represents the normalized amplitude coefficient;  $k_{zl} \approx \sqrt{k^2 - ((|l|+2)/r_l)^2}$  and  $k_{zl}(z) \approx \sqrt{k^2 - ((|l|+2)/r_l(z))^2}$  denotes the customized longitudinal wavevector component;  $\hat{x}, \hat{y}, \hat{r}, \hat{\phi}$  are the unit vectors in Cartesian and cylindrical coordinates, respectively; the single prime symbol denoting the first-order derivative with respect to z, e. g.,  $r'_l(z), r_l'(z), x'_s(z), y'_s(z)$  and  $I'(z)$ . The constant  $C$  in the fourth row is a positive constant, as will be discussed in Method 3.

## 2. Experimental Generation and Tomography for Multimodal NDPVB.

**Generation.** A reflective phase-only spatial light modulator imprinted with computer-generated hologram patterns transforms a collimated laser light wave into the complex field  $S(k_r, \phi, k_z)$ , with help of spatial filtering via a 4-F system consisting of lenses L1 and L2, and an iris as well (Fig. 7). The resulting field is responsible for multimodal NDPVB in the focal volume of lens L3. It should be noted that in the real-space coordinate system, the radial wavenumber  $k_r$  must be converted into the radial coordinate in the incident plane (i.e. the front focal plane) according to the relation  $k_r = kr/f$ .

**Tomography.** A delay line, consisting of a right-angle and a hollow-roof prism mirrors and a translation stage, enables the different cross-sections of multimodal NDPVBs to be imaged on a CMOS camera after a relay 4-F system consisting of two lenses (L4 and L5). The combination of the delay line and

the relay system (Fig. 7) enables us to record intensity cross sections at different z-axial locations in the focal volume of lens L3. (The actual experimental apparatus provided in Supplementary Note 3)

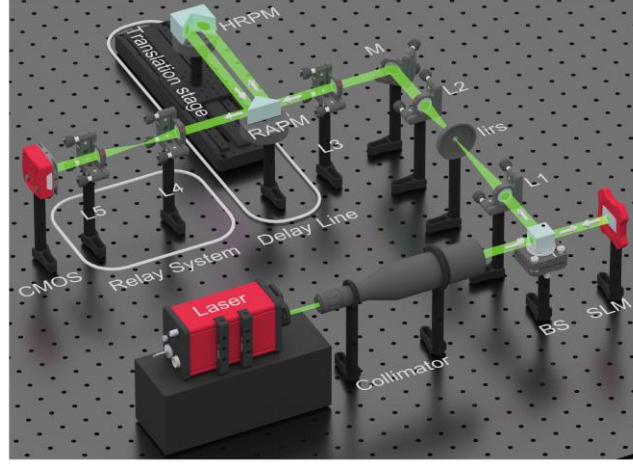


**Fig. 7. Experimental setup for Generation and Tomography of Multimodal NDPVB.** BS, beam splitter; SLM, phase-only spatial light modulator; L1-L5, lens; M, mirror; RAPM, right-angle prism mirror; HRPM, hollow roof prism mirror (LBTEK HRM25-AG).

### 3. Streamline Interaction Manipulation by Optical “Fluid-Continuity Equation”.

The propagation of optical energy in a beam can be described by optical “Fluid-Continuity Equation”<sup>36</sup> (namely, Transport of Intensity Equation<sup>63</sup>), read as:

$$\frac{\partial W(r, \varphi, z)}{\partial z} = -c(\nabla_{\perp} \mathbf{p}_{\perp}(r, \varphi, z)), \quad (6)$$

where  $W(r, \varphi, z)$  is the energy density,  $\mathbf{p}_{\perp}(r, \varphi, z)$  the transverse energy-flow (momentum) density,  $\nabla_{\perp}$  denotes the transverse divergence operator, and  $c$  is the velocity of light. This relationship indicates that the transverse energy-flow (momentum) density  $\mathbf{p}_{\perp}(r, \varphi, z)$ , influences the propagation of optical energy density  $W(r, \varphi, z)$ . If one treats  $W$  as a fluid density field and  $\mathbf{p}_{\perp}$  as the corresponding transverse velocity field, Eq. (6) becomes exactly the continuity equation of incompressible-fluid dynamics, enforcing conservation of matter.

Non-diffracting perfect-vortex beams (NDPVBs) feature an invariant mainlobe, regardless of topological charge  $\ell$  or propagation distance  $z$ . We therefore decompose these beams into two regions: mainlobe (region of interest): the high-intensity region that interacts directly with matter or detectors; sidelobes: a concentric series of rings that sustain and regulate the mainlobe’s propagation. During free-space propagation, energy streamlines of standard NDPVB in these two regions  $\{r, \varphi_0 + \ell/(r^2 k_{zl})z, z\}$ , circulate on distinct cylindrical surfaces without exchanging energy. However, by invoking Eq. (6), we can actively couple the sidelobes to the mainlobe as an on-demand energy reservoir.

Considering the ring area of the mainlobe at  $r=r$ , the derivative  $\partial W(r, \varphi, z)/\partial z$  is directly proportional to  $\partial I(z)/\partial z = I'(z)$ . The divergence of transverse energy flow or momentum density,  $\nabla_{\perp} \mathbf{p}_{\perp}(r, \varphi, z)$ , can be equated to the flux of transverse energy flow across the ring. Owing to the beam’s perfect axisymmetry,

azimuthal flows circulate within the ring and do not contribute to net flux; only the radial component matters. Hence, the radial energy flow exhibits a direct correlation with  $-I'(z_0)$ , donated as  $-CI'(z_0)$  with the integrated positive constant  $C$  (Raw 4, Table 1). When  $I'(z) > 0$ , the negative sign in radial energy flow indicates an inward radial flow: sidelobe streamlines converge into the mainlobe, replenishing and amplifying its energy (see Fig. 3C). When  $I'(z) < 0$ , the flow reverses, allowing controlled depletion of the mainlobe back into the sidelobes.

By programming the spatial light modulator to impose a desired axial energy gradient  $I'(z)$ , one gains *continuous, bidirectional* control over the sidelobe-to-mainlobe energy transfer rate. This tunability enables:

1. Enhanced local intensity—by funneling nearly all sidelobe energy inward, one can boost detector signal-to-noise and overall energy efficiency (Fig. 3C, a three-fold improvement is detailed in Supplementary Note 6).
2. Attenuation compensation—by matching the sidelobe streamlines inflow rate to medium-induced decay, the mainlobe's intensity remains constant during propagating (Figs. 3G–J).

In this way, the sidelobes serve not only as passive scaffolding for self-healing (Fig. 3A) but also as an *actively addressable energy reservoir* for precision-tailored structured-light applications (Figs. 3G–J).

## Acknowledgements

## Reference

1. Forbes, A., De Oliveira, M. & Dennis, M. R. Structured light. *Nat. Photonics* **15**, 253–262 (2021).
2. Bliokh, K. Y. *et al.* Roadmap on structured waves. *J. Opt.* **25**, 103001 (2023).
3. Kogelnik, H. & Li, T. Laser beams and resonators. *Proc. IEEE* **54**, 1312–1329 (1966).
4. Gutiérrez-Vega, J. C. & Bandres, M. A. Helmholtz–Gauss waves. *J. Opt. Soc. Am. A* **22**, 289 (2005).
5. Durnin, J., Miceli, J. J. & Eberly, J. H. Diffraction-free beams. *Phys. Rev. Lett.* **58**, 1499–1501 (1987).
6. Bencheikh, A. *et al.* Cosine beam: diffraction-free propagation and self-healing. *J. Opt. Soc. Am. A* **37**, C7 (2020).
7. Gutiérrez-Vega, J. C., Iturbe-Castillo, M. D. & Chávez-Cerda, S. Alternative formulation for invariant optical fields: Mathieu beams. *Opt. Lett.* **25**, 1493 (2000).
8. Bandres, M. A., Gutiérrez-Vega, J. C. & Chávez-Cerda, S. Parabolic nondiffracting optical wave fields. *Opt. Lett.* **29**, 44 (2004).
9. Berry, M. V. & Balazs, N. L. Nonspreading wave packets. *American Journal of Physics* **47**, 264–267 (1979).
10. Siviloglou, G. A. & Christodoulides, D. N. Accelerating finite energy Airy beams. *Opt. Lett.* **32**, 979 (2007).
11. Siviloglou, G. A., Broky, J., Dogariu, A. & Christodoulides, D. N. Observation of Accelerating Airy Beams. *Phys. Rev. Lett.* **99**, 213901 (2007).
12. Efremidis, N. K., Chen, Z., Segev, M. & Christodoulides, D. N. Airy beams and accelerating waves: an overview of recent advances. *Optica* **6**, 686 (2019).
13. *Self-Focusing: Past and Present: Fundamentals and Prospects*. vol. 114 (Springer New York, New York, NY, 2009).
14. Allen, L., Beijersbergen, M. W., Spreeuw, R. J. C. & Woerdman, J. P. Orbital angular momentum of light and the transformation of Laguerre-Gaussian laser modes. *Phys. Rev. A* **45**, 8185–8189 (1992).
15. Coulet, P., Gil, L. & Rocca, F. Optical vortices. *Optics Communications* **73**, 403–408 (1989).

16. Yang, Y., Ren, Y.-X. & Rosales-Guzmán, C. *Optical Vortices: Fundamentals and Applications*. (IOP Publishing, 2024). doi:10.1088/978-0-7503-5844-6.
17. Shen, Y. *et al.* Optical vortices 30 years on: OAM manipulation from topological charge to multiple singularities. *Light Sci. Appl.* **8**, 90 (2019).
18. Willner, A. E. *et al.* Design challenges and guidelines for free-space optical communication links using orbital-angular-momentum multiplexing of multiple beams. *J. Opt.* **18**, 074014 (2016).
19. Xie, G. *et al.* Performance metrics and design considerations for a free-space optical orbital-angular-momentum-multiplexed communication link. *Optica*, **2**, 357–365 (2015).
20. Li, M., Yan, S., Zhang, Y., Zhou, Y. & Yao, B. Orbital angular momentum in optical manipulations. *J. Opt.* **24**, 114001 (2022).
21. Krenn, M. Communication with spatially modulated light through turbulent air across Vienna. *New J. Phys.* (2014) **16**(11): 113028.
22. Krenn, M. *et al.* Twisted light transmission over 143 km. 2016, **113**(48): 13648-13653.
23. Cheng, M., Jiang, W., Guo, L., Li, J. & Forbes, A. Metrology with a twist: probing and sensing with vortex light. *Light Sci. Appl.* **14**, 4 (2025).
24. Phillips, R. L. & Andrews, L. C. Spot size and divergence for Laguerre Gaussian beams of any order. *Appl. Opt.*, **22**, 643–644 (1983).
25. Vaity, P. & Rusch, L. Perfect vortex beam: Fourier transformation of a Bessel beam. *Opt. Lett.* **40**, 597 (2015).
26. Yan, W. *et al.* Energy-flow-reversing dynamics in vortex beams: OAM-independent propagation and enhanced resilience. *Optica* **11**, 531 (2024).
27. Yan, W. *et al.* Iso-propagation vortices with OAM-independent size and divergence toward future faster optical communications. *Adv. Photon.* **6**(3): 036002-036002 (2024).
28. Graham, R. & Haken, H. Laserlight first example of a second-order phase transition far away from thermal equilibrium. *Z. Physik* **237**, 31–46 (1970).
29. Aranson, I. S. & Kramer, L. The world of the complex Ginzburg-Landau equation. *Rev. Mod. Phys.* **74**, 99–143 (2002).
30. Couillet, P., Gil, L. & Lega, J. Defect-mediated turbulence. *Phys. Rev. Lett.* **62**, 1619–1622 (1989).
31. Brambilla, M. *et al.* Transverse laser patterns. I. Phase singularity crystals. *Phys. Rev. A* **43**, 5090–5113 (1991).
32. Brambilla, M. *et al.* Transverse laser patterns. II. Variational principle for pattern selection, spatial multistability, and laser hydrodynamics. *Phys. Rev. A* **43**, 5114–5120 (1991).
33. Rosanov, N. N., Fedorov, S. V. & Shatsev, A. N. Curvilinear Motion of Multivortex Laser-Soliton Complexes with Strong and Weak Coupling. *Phys. Rev. Lett.* **95**, 053903 (2005).
34. Genevet, P., Barland, S., Giudici, M. & Tredicce, J. R. Bistable and Addressable Localized Vortices in Semiconductor Lasers. *Phys. Rev. Lett.* **104**, 223902 (2010).
35. Barland, S. *et al.* Observation of “True” Optical Vortices in a Laser System. in *Nonlinear Photonics and Novel Optical Phenomena* (eds. Chen, Z. & Morandotti, R.) vol. 170 195–205 (Springer New York, New York, NY, 2012).
36. Bekshaev, A., Bliokh, K. Y. & Soskin, M. Internal flows and energy circulation in light beams. *J. Opt.* **13**, 053001 (2011).
37. Berry, M. V. & McDonald, K. T. Exact and geometrical optics energy trajectories in twisted beams. *J. Opt. A: Pure Appl. Opt.* **10**, 035005 (2008).
38. Bliokh, K. Y., Bekshaev, A. Y., Kofman, A. G. & Nori, F. Photon trajectories, anomalous velocities and

- weak measurements: a classical interpretation. *New J. Phys.* **15**, 073022 (2013).
39. Kocsis, S. *et al.* Observing the Average Trajectories of Single Photons in a Two-Slit Interferometer. *Science* **332**, 1170–1173 (2011).
  40. Padgett, M. J. & Allen, L. The Poynting vector in Laguerre-Gaussian laser modes. *Optics Communications* **121**, 36–40 (1995).
  41. Madelung, E. Quantentheorie in hydrodynamischer Form. *Z. Physik* **40**, 322–326 (1927).
  42. Holland, P. R. *The Quantum Theory of Motion: An Account of the de Broglie-Bohm Causal Interpretation of Quantum Mechanics*. (Cambridge University Press, 1993).
  43. Bohm, D., Hiley, B. J. & Kaloyerou, P. N. An ontological basis for the quantum theory. *Physics Reports* **144**, 321–375 (1987).
  44. Mendoza-Hernández, J., Hidalgo-Aguirre, M., Ladino, A. I. & Lopez-Mago, D. Perfect Laguerre–Gauss beams. *Opt. Lett.*, **45**, 5197–5200 (2020).
  45. Ghosh, B. *et al.* Canonical and Poynting currents in propagation and diffraction of structured light: tutorial. *J. Opt. Soc. Am. B* **41**, 1276 (2024).
  46. Dabiri, D. & Pecora, C. Introduction. in *Particle Tracking Velocimetry* (IOP Publishing, 2019).
  47. Yang, Y., Ren, Y.-X., Chen, M., Arita, Y. & Rosales-Guzmán, C. Optical trapping with structured light: a review. *Adv. Photon.* **3**, 2021, 3(3): 034001-034001.
  48. Liang, Y. *et al.* Simultaneous optical trapping and imaging in the axial plane: a review of current progress. *Rep. Prog. Phys.* **83**, 032401 (2020).
  49. Jia, Q. *et al.* Optical manipulation: from fluid to solid domains. *Photonics Insights* **2**, R05 (2023).
  50. Shannon, C. E. A mathematical theory of communication. *The Bell System Technical Journal* **27**, 379–423 (1948).
  51. Evangelides, S. G., Mollenauer, L. F., Gordon, J. P. & Bergano, N. S. Polarization multiplexing with solitons. *Journal of Lightwave Technology* **10**, 28–35 (1992).
  52. *Optical WDM Networks*. (Kluwer Academic Publishers, Boston, 2006).
  53. Wang, J. *et al.* Terabit free-space data transmission employing orbital angular momentum multiplexing. *Nature Photon.* **6**, 488–496 (2012).
  54. Wan, Z. *et al.* Divergence-degenerate spatial multiplexing towards future ultrahigh capacity, low error-rate optical communications. *Light Sci. Appl.* **11**, 144 (2022).
  55. Wang, J. *et al.* Orbital angular momentum and beyond in free-space optical communications. *Nanophotonics* **11**, 645–680 (2022).
  56. Zhao, N., Li, X., Li, G. & Kahn, J. M. Capacity limits of spatially multiplexed free-space communication. *Nature Photon.* **9**, 822–826 (2015).
  57. Klug, A., Nape, I. & Forbes, A. The orbital angular momentum of a turbulent atmosphere and its impact on propagating structured light fields. *New J. Phys.* **23**, 093012 (2021).
  58. Willner, A. E. *et al.* Utilizing Structured Modal Beams in Free-Space Optical Communications for Performance Enhancement. *IEEE J. Select. Topics Quantum Electron.* **29**, 1–13 (2023).
  59. Zannotti, A., Denz, C., Alonso, M. A. & Dennis, M. R. Shaping caustics into propagation-invariant light. *Nat Commun.* **11**, 3597 (2020).
  60. Yan, W. *et al.* Non-diffracting and self-accelerating Bessel beams with on-demand tailored intensity profiles along arbitrary trajectories. *Opt. Lett.* **46**, 1494 (2021).
  61. Li, Y. *et al.* Flexible trajectory control of Bessel beams with pure phase modulation. *Opt. Express* **30**, 25661 (2022).
  62. Goutsoulas, M., Bongiovanni, D., Li, D., Chen, Z. & Efremidis, N. K. Tunable self-similar Bessel-like

beams of arbitrary order. *Opt. Lett.* **45**, 1830 (2020).

63. Zuo, C. *et al.* Transport of intensity equation: a tutorial. *Optics and Lasers in Engineering* **135**, 106187 (2020).
64. Yan W, Gao Y, Yuan Z, et al. Versatile Non-diffracting Perfect Vortex Beams. arXiv preprint arXiv:2209.00481, 2022.